High-pressure synthesis of the cubic perovskite $BaRuO_3$ and evolution of ferromagnetism in $ARuO_3$ (A = Ca, Sr, Ba) ruthenates

C.-Q. Jin[†‡], J.-S. Zhou[§], J. B. Goodenough[§], Q. Q. Liu[†], J. G. Zhao[†], L. X. Yang[†], Y. Yu[†], R. C. Yu[†], T. Katsura[¶], A. Shatskiy[¶], and E. Ito[¶]

[†]Institute of Physics, Chinese Academy of Science, Beijing 100080, China; [§]Texas Materials Institute, University of Texas, Austin, TX 78712; and [¶]Institute for Study of the Earth's Interior, Okayama University, Misasa, Tottori, 682-0193, Japan

Edited by Ho-kwang Mao, Carnegie Institution of Washington, Washington, DC, and approved March 7, 2008 (received for review November 18, 2007)

The cubic perovskite $BaRuO_3$ has been synthesized under 18 GPa at 1,000°C. Rietveld refinement indicates that the new compound has a stretched Ru–O bond. The cubic perovskite $BaRuO_3$ remains metallic to 4 K and exhibits a ferromagnetic transition at $T_c = 60$ K, which is significantly lower than the $T_c \approx 160$ K for $SrRuO_3$. The availability of cubic perovskite $BaRuO_3$ not only makes it possible to map out the evolution of magnetism in the whole series of $ARuO_3$ (A = Ca, Sr, Ba) as a function of the ionic size of the A-site r_A, but also completes the polytypes of $BaRuO_3$. Extension of the plot of T_c versus r_A in perovskites $ARuO_3$ (A = Ca, Sr, Ba) shows that T_c does not increase as the cubic structure is approached, but has a maximum for orthorhombic $SrRuO_3$. Suppressing T_c by Ca and Ba doping in $SrRuO_3$ is distinguished by sharply different magnetic susceptibilities $\chi(T)$ of the paramagnetic phase. This distinction has been interpreted in the context of a Griffiths' phase on the (Ca Sr)RuO_3 side and bandwidth broadening on the (Sr,Ba)RuO_3 side.

magnetism | compounds | Ruthenate

Transition-metal oxides with perovskite (1) and perovskite-related compounds have been extensively studied in recent years; for example, high-T_c superconductivity in copper oxides, the colossal magnetoresistance effect in manganese oxides, and more recently multiferroic phenomena. Because perovskite has a densely packed crystal structure (2), high-pressure synthesis, which is widely used in the field of geoscience for studying the lower mantle, is very effective and critical, in some cases, to synthesize compounds with the perovskite structure (3). Application of the high-pressure technique enables us to explore new perovskites that are not formed under ambient pressure and have unknown physical properties.

The ruthenium oxides with perovskite-related structure have received growing attention because they exhibit physical properties such as a superconductivity in Sr_2RuO_4 (4), the metamagnetic metallic behavior of $Sr_3Ru_2O_7$ (5), and quantum phase transitions in $BaRu_6O_{12}$ (6). The perovskites $ARuO_3$ (A = Sr, Ca) are technically important materials as a conducting buffer layer in electronic devices. Moreover, the cause of the unusual disappearance of ferromagnetism in the $Sr_{1-x}Ca_xRuO_3$ is currently under hot debate. In the orthorhombic perovskite with Pbnm space group shown in Fig. 1*a*, the magnetic coupling in these $ARuO_3$ (A = Ca and Sr) perovskites is determined by the Ru–O–Ru bond angle and Ru–O covalent bonding. $CaRuO_3$ remains paramagnetic to the lowest temperature (7, 8), but it is near the verge of ferromagnetic order (9, 10). However, $SrRuO_3$ is an itinerant-electron ferromagnet with a $T_c \approx 164$ K (11–16). As a representation of currently popular models about the ferromagnetism in $SrRuO_3$, Mazin and Singh (17) have calculated the band structure of $Sr_{1-x}Ca_xRuO_3$ by taking into account the cooperative RuO_6 site rotation that bends the Ru–O–Ru bond angle from 163° in $SrRuO_3$ to148° in $CaRuO_3$; they found that the increased bending of the Ru–O–Ru bond angle reduces the band degeneracy and, therefore, the density of electronic states at the Fermi energy $\rho(\varepsilon_F)$, perhaps to where the Stoner criterion $\rho(\varepsilon_F)U \approx 1$, where $\rho(\varepsilon_F)$ is the electron at the Fermi energy and U is the electron correlation energy, is no longer valid in $CaRuO_3$. This model predicts that the maximum T_c will be achieved as the high-symmetry cubic structure is approached because a higher $\rho(\varepsilon_F)$ is created at high-symmetry points in the Brillouin zone. The striking difference of the magnetic properties between $SrRuO_3$ and $CaRuO_3$ makes cubic perovskite $BaRuO_3$ an interesting candidate since an ideal cubic perovskite is expected because of the larger A-site ionic radius. Mapping out the evolution of the magnetism for the whole perovskite series of $ARuO_3$ from A = Ca across Sr to Ba will shed a new light on the mysterious itinerant-electron ferromagnetism in these ruthenates. However, a literature search shows that $BaRuO_3$ has polytype structures (18–20) depending on how it is synthesized, i.e., the nine-layered rhombohedral (9L), the four-layered hexagonal (4H), and the six-layered hexagonal (6H) as shown in Fig. 1*b*. All of these polytype structures can be described by different stacking sequences of RuO_6 octahedra along the *c* axis. High-pressure synthesis of an AMO_3 compound as a cubic perovskite is necessary where the mismatch between the equilibrium (A–O) and (M–O) bond lengths gives a tolerance factor $t \equiv (\text{A–O})/\sqrt{(\text{M–O})} > 1$. The perovskite structure can accommodate a $t < 1$ by a cooperative rotation of the corner-shared MO_6 octahedra, which bends the M–O–M bond angle from 180° to (180° − ϕ) and lowers the symmetry from cubic, but it accommodates to a $t > 1$ by forming hexagonal polytypes (3). Tabulated ionic radii (21) give room-temperature $BaRuO_3$ a $t = 1.0625$, and it crystallizes as a 9R polytype with close-packed BaO_3 layers stacked cubic-hexagonal-hexagonal-cubic. . .along the *c* axis. Because the (M–O) bond is less compressible than the (A–O) bond for most $A^{2+}M^{4+}O_3$ compounds (3), pressure reduces *t*. Therefore, sintering under high pressure results in the structure sequence in $BaRuO_3$ from 9R to 4H and to 6H polytypes as reported in the literature. The end member in this family, the perovskite structure (3C), could not be synthesized under the highest pressure available in early days. Here, we report that the perovskite $BaRuO_3$ can be obtained under 18 GPa at 1,000°C, nearly the same pressure found at the boundary of the Earth's Upper and Lower mantle. The new compound has the cubic perovskite structure with space group Pm-3m.

Results and Discussion

Fig. 1*c* shows that all x-ray diffraction peaks of the high-pressure product under 18 GPa of $BaRuO_3$ can be indexed with cubic

Author contributions: C.-Q.J., J.-S.Z., and Q.Q.L. designed research; Q.Q.L., J.G.Z., L.X.Y., Y.Y., R.C.Y., and A.S. performed research; T.K. and E.I. contributed new reagents/analytic tools; C.-Q.J., J.-S.Z., J.B.G., and Q.Q.L. analyzed data; and C.-Q.J., J.-S.Z., and J.B.G. wrote the paper.

The authors declare no conflict of interest.

This article is a PNAS Direct Submission.

[‡]To whom correspondence should be addressed. E-mail: jin@aphy.iphy.ac.cn.

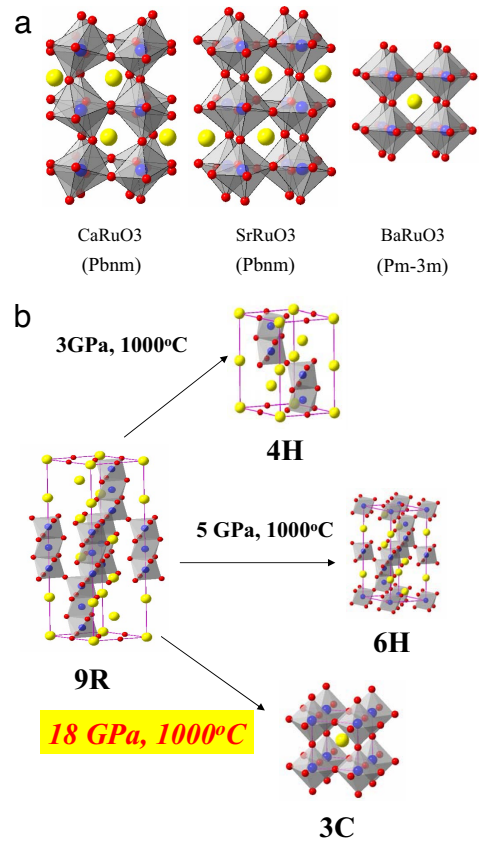

Fig. 1. The crystallography of $ARuO_3$. (*a*) Schematic drawing of the three perovskites $CaRuO_3$, $SrRuO_3$, and $BaRuO_3$ where red balls stand for O, blue balls for Ru, and yellow balls for alkaline earth Ca, Sr, and Ba. (*b*) The crystal structures of the $BaRuO_3$ polytypes. Blocks of the face-shared and corner-shared RuO_6 octahedra are stacked alternately along the *c* axis. (*c*) X-ray powder diffraction spectra of the perovskites $CaRuO_3$, $SrRuO_3$, and $BaRuO_3$ and their best fit with the Rietveld analysis at room temperature.

perovskite structure of space group Pm-3m. Results of Rietveld analysis of the x-ray diffraction for perovskite ruthenates $ARuO_3$ (A = Ca, Sr, Ba) are given in Table 1, which illustrates a systematical structural change from $CaRuO_3$ to $SrRuO_3$ and to $BaRuO_3$. The significant structural changes as a function of r_A include (*i*) the bending of the $(180° - \phi)$ Ru–O–Ru bonds decreases from 148.6° in $CaRuO_3$ to 162.6 ° in $SrRuO_3$ and finally to 180° in cubic $BaRuO_3$; (*ii*) the (Ru–O) bond length $d = 2.003$ Å in cubic $BaRuO_3$ is slightly stretched in comparison with the

Table 1. Results of the Rietveld refinement of the x-ray diffraction of Fig.1*c*

	$CaRuO_3$ (Orthorhombic)	$SrRuO_3$ (Orthorhombic)	$BaRuO_3$ (Cubic)
Space group	Pnma(62)	Pnma(62)	Pm-3m(221)
a, Å	5.35744(3)	5.57108(4)	4.0059(2)
b, Å	5.53298(3)	5.53543(4)	
c, Å	7.66333(4)	7.85040(7)	
Ru-O_1 (Å) ×2	1.9909(4)	1.9842(7)	2.0029
Ru-O_2 (Å) ×2	2.000(3)	1.986(7)	
Ru-O_2 (Å) ×2	1.997(2)	1.988(6)	
Ru-O_1-Ru, °	148.60(2)	163.08(3)	180
Ru-O_2-Ru, °	148.7(1)	162.4(3)	
$R_{p,}$ %	8.19	5.9	7.6
χ^2	3.1	2.3	2.5

average Ru–O bond length $d = 1.986$ Å in $SrRuO_3$ and $d = 1.996$ Å in $CaRuO_3$; (*iii*) the octahedral-site distortion as measured by the difference between three Ru–O bond lengths becomes more obvious in $CaRuO_3$, but it remains within the level of intrinsic structural distortion generally found in the orthorhombic perovskite structure with Pbnm space group. The cubic $BaRuO_3$ is stable down to 10 K as checked by x-ray diffraction.

The transport properties of Fig. 2 show that cubic $BaRuO_3$ remains metallic down to 4.2 K. However, the ferromagnetic transition temperature T_c is 60 K, ≈100 K lower than that of $SrRuO_3$, and the saturation magnetization at 5 K in a magnetic field of 5 Tesla remains near 0.8 μ_B/Ru, far <2.0 μ_B/Ru expected for a localized electron-spin-only moment for low-spin Ru(IV):t^4e^0 and significantly lower than the 1.4 μ_B/Ru in $SrRuO_3$. A small substitution of Ba for Sr in $Sr_{1-y}Ba_yRuO_3$ does not change the magnetization at 5 K; it remains ≈1.4 μ_B/Ru. However, the effective magnetic moment $\mu_{eff} \approx 2.6$ μ_B/Ru calculated from the paramagnetic phase, which is close to the spin-only 2.8 μ_B/Ru for S = 1, is similar for all of the Ba doped

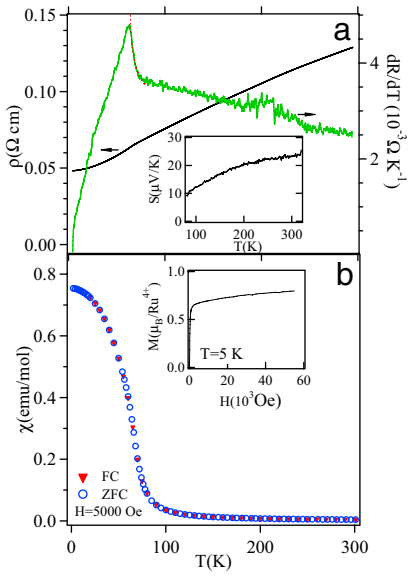

Fig. 2. The primary electric and magnetic properties of $BaRuO_3$ cubic perovskite. (*a*) Temperature dependence of the resistivity ρ and its derivative $d\rho/dT$ of cubic $BaRuO_3$; dashed line on the curve $d\rho/dT$ vs. *T* is a curve fitting to the formula $|(T - T_c)/T_c|^{-\alpha}$, $\alpha = 0.11$. (*Inset*) Shown is the temperature dependence of thermoelectric power. (*b*) Temperature dependence of the molar magnetic susceptibility of perovskite $BaRuO_3$. (*Inset*) Shown is the magnetization at 5 K.

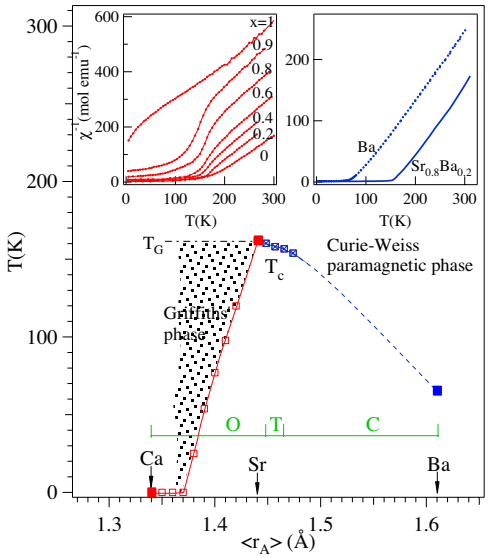

Fig. 3. Phase diagram of the magnetic transition temperatures versus the tabulated average A-site ionic radius $\langle r_A \rangle$ for $Sr_{1-y}Ba_yRuO_3$ and $Sr_{1-x}Ca_xRuO_3$. Three members in the phase diagram $CaRuO_3$, $SrRuO_3$, and $BaRuO_3$, in which the A-site size variance is zero, are distinguished by the solid symbols. The shaded area in the phase diagram represents the phase having the characteristic $\chi^{-1}(T)$ of the Griffiths' phase. Letters inside the diagram stand for the crystal structure as determined by x-ray diffraction at room temperature, O for orthorhombic, T for tetragonal, and C for cubic. (*Inset*) Temperature dependence of inverse magnetic susceptibility of $Sr_{1-x}Ca_xRuO_3$ measured with a magnetic field H = 1 T (data are from ref. 28) and of $Sr_{1-y}Ba_yRuO_3$ measured with a magnetic field H = 0.5 T in this work.

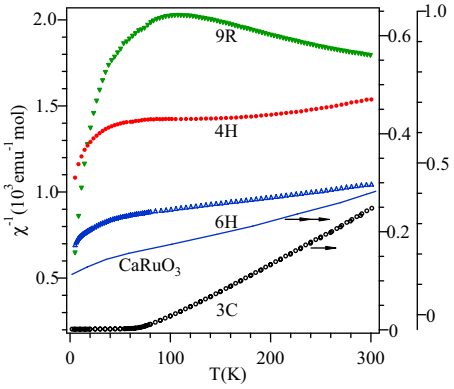

Fig. 4. Pressure dependence of the ferromagnetic transition temperature T_c in cubic $BaRuO_3$. The dashed line is from the prediction of an itinerant-electron ferromagnetism model (34). $T_c \approx (P_c - P)^{1/2}$, where P_c (P_c = 5 GPa is used in the plotting) is the critical pressure where T_c vanishes.

$Sr_{1-y}Ba_yRuO_3$ perovskites in this study. The thermoelectric power $S(T)$ (Fig. 2 *Inset*) of the perovskite $BaRuO_3$ is nearly identical to that of $CaRuO_3$ (22) and it is ≈5 μV/K smaller than that of $SrRuO_3$ at room temperature (15). We have fit $d\rho/dT$ of $BaRuO_3$ in the vicinity of T_c with the scaling law $|(T - T_c)/T_c|^{-\alpha}$. The fitting for $T \rightarrow T_c$ from above gives an $\alpha = 0.11$, which matches well theoretical prediction for itinerant-electron ferromagnetism (23). However, the law fails to describe $d\rho/dT$ as $T \rightarrow T_c$ from below. Beyond the critical spin-fluctuation range near T_c, however, $\rho(T)$ of $BaRuO_3$ shows a temperature dependence similar to that of $SrRuO_3$ below and above T_c. As T approaches 4.2 K, $\rho(T)$ is described by the power law $\rho(T) - \rho(0) \sim T^2$, indicating a Fermi-liquid character. The availability of $Sr_{1-y}Ba_yRuO_3$ with perovskite structure and the literature data for well studied $Ca_{1-x}Sr_xRuO_3$ allows us to map out completely T_c versus $\langle r_A \rangle$ for the whole family of $ARuO_3$ perovskites as shown in Fig. 3. Interestingly, T_c peaks out at $\langle r_A \rangle \approx r_{Sr}$ where it remains within the orthorhombic phase. A preliminary result shows that the transition to a cubic phase occurs at $y \approx 0.15$ in $Sr_{1-y}Ba_yRuO_3$. For the compositions with Ba doping $y > 0.15$, the Ru–O bond is stretched from its equilibrium value. One should keep in mind that the size variance (i.e., the composition combination) induced by Ca or Ba doping will also reduce the magnetic transition temperature T_c as has been demonstrated (24). This effect, however, has little to do with a complete suppression of the ferromagnetic transition in $CaRuO_3$ and a dramatic reduction of T_c in cubic $BaRuO_3$. The symmetry argument as mentioned in the introduction also does not work because T_c is reduced in cubic $BaRuO_3$. To identify the mechanism of T_c suppression beyond the size variance induced by the Ca and Ba doping on both sides of $SrRuO_3$, we made a comparison between two compositions of $Sr_{1-x}Ca_xRuO_3$ and $Sr_{1-y}Ba_yRuO_3$ with approximately the same $\sigma^2 = (\langle r_A^2 \rangle - \langle r_A \rangle^2)$ (a measure to define size variance) (24). As a matter of fact, all compositions of $Sr_{1-y}Ba_yRuO_3$, including $y = 0$, show typical Curie–Weiss (CW) behavior at $T > T_c$ and Gaussian or critical fluctuations in the vicinity of T_c, whereas compositions of $Sr_{1-x}Ca_xRuO_3$ show an unusual $\chi^{-1}(T)$ as T_c is approached in the paramagnetic phase, as is shown in Fig. 3 *Inset*. It is clear that the T_c reductions in $Sr_{1-x}Ca_xRuO_3$ and $Sr_{1-y}Ba_yRuO_3$ appear to be caused by different mechanisms.

On the $Sr_{1-y}Ba_yRuO_3$ ($y \geq 0$) side, T_c reduction is likely caused by band broadening in a uniform ferromagnetic system because a well defined CW paramagnetism is found at $T > T_c$ (25). Ba doping could change the bandwidth through two opposite effects. Because the A–O interaction in a perovskite $ARuO_3$ competes with the Ru^{4+} ions for the O-2p_π electrons, the stronger ionic character of the Ba^{2+}, which makes it less competitive for the O-2p orbitals, enhances the covalent admixture of O:2p_π character into the π^* bands of primarily 4d-electron character, therefore broadening the bandwidth W associated with the Ru–O bond. However, the Ba doping for $y > 0.15$ in the cubic perovskite phase stretches the Ru–O bond length as obtained from the Rietveld refinement of this work, which reduces the bandwidth. To distinguish which effect plays the dominant role in controlling the bandwidth, we have carried out a structure study and measurement of T_c under pressure on the cubic $BaRuO_3$, as shown in Fig. 4. Pressure does not alter the fact that Ba^{2+} has strong ionic character, but it does change the Ru–O bond length. The cubic phase is stable up to 100 kbar, the maximum pressure used in this study, and the Ru–O bond length shortens continuously under pressure. T_c drops at a rate $dT_c/dP \approx 0.7$ K/kbar at low pressures, which is similar to that of $SrRuO_3$ (26) and then gradually approaches a saturated $T_c \approx 50$ K at $P > 20$ kbar. The saturation T_c at high pressures in the cubic $BaRuO_3$ is lower than that of thin-film $SrRuO_3$ found for $P > 130$ kbar (27). This observation indicates unambiguously that the strong ionic character of Ba^{2+} broadens W; the broadening is offset slightly by a stretched Ru–O bond length in cubic $BaRuO_3$. High pressure decreases T_c by reducing the Ru–O bond length. It requires a much higher pressure in $SrRuO_3$ than that in the $BaRuO_3$ to lower T_c to a saturation value. The saturation of T_c vs. P curve in both $SrRuO_3$ and the cubic $BaRuO_3$ suggests there is a critical W above which there may be a first-order transition to a Pauli paramagnetic phase. The bandwidth broadening by Ba doping reduces the density of states $\rho(\varepsilon_F)$ near the Fermi energy and, therefore, T_c according to the Stoner model.

In sharp contrast, $\chi^{-1}(T)$ for all $Sr_{1-x}Ca_xRuO_3$ ($x > 0$) deviates from the CW law at a $T \approx T_c$ of $SrRuO_3$ with a curvature that is opposite to that caused by critical fluctuations shown in the vicinity of T_c for $Sr_{1-y}Ba_yRuO_3$. T_c reduction and the final vanishing in $Sr_{1-x}Ca_xRuO_3$ appears to be correlated to the anomalous paramagnetic susceptibility. The peculiar $\chi^{-1}(T)$ for all $Sr_{1-x}Ca_xRuO_3$

GEOLOGY

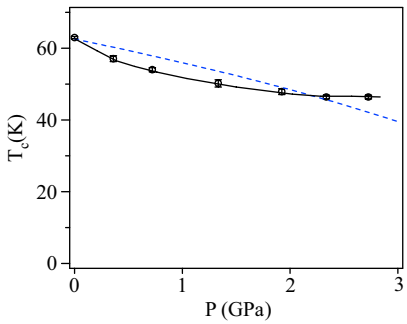

Fig. 5. Temperature dependences of the inverse magnetic susceptibility of the 9R, 4H, 6H, and 3C phases of $BaRuO_3$. The $\chi^{-1}(T)$ data of the perovskite $CaRuO_3$ are superimposed for comparison.

($x > 0$) (28) is characteristic of a diluted ferromagnetic system (29) in which Griffiths (30) has predicted a nonanalytic $\chi^{-1}(T)$ below a $T_G = T_c$ of the undiluted parent phase. Moreover, the phase diagram of T_c vs. x on the side of $Sr_{1-x}Ca_xRuO_3$ matches stunningly well to the prediction based on the model for a diluted Heisenberg ferromagnet (31). The implication of these observations is straightforward: suppression of T_c in $Sr_{1-x}Ca_xRuO_3$ has little to do with either reducing the $\rho(\varepsilon_F)$ or a competition between ferromagnetic and antiferromagnetic interactions, but is caused by the dilution of ferromagnetic spin–spin coupling across Ru–O–Ru bonds. A thorough study of the magnetic property of the $BaRuO_3$ from the whole series of hexagonal polytypes to the 3C phases helps us to clarify this long-standing puzzle.

The systematic change in the magnetic susceptibility of the polytype phases of $BaRuO_3$ is shown in Fig. 5. The change of $\chi(T)$ can be easily correlated with the characteristics of the polytype structures, which consist of face shared (F) and corner shared (C) RuO_6 octahedra. These shared interfaces repeat as CFFCFFCFF, CFCF, FCCFCC, and CCC along the c axis from the 9R, 4H, 6H, to 3C phases. On crossing these interfaces, two Ru–Ru bonds can be defined, i.e., a $\theta = 180°$ Ru–[C]–Ru bond of ≈3.9 Å and a $\theta \approx 135°$ Ru–[F]–Ru bond of ≈2.55 Å. The metallic 9R phase shows no magnetic ordering and exhibits neither a CW law nor Pauli paramagnetic susceptibility. Changing the balance of Ru–[F]–Ru bonds vs. Ru–[C]–Ru bonds from the 9R, 4H, 6H, and finally to the 3C phase makes the $\chi^{-1}(T)$ evolve from a wiggled curve to the CW law. The relationship between the structural features and a systematic change of $\chi^{-1}(T)$ suggests that the Ru–[C]–Ru bond is dominated by the spin–spin interaction, whereas the Ru–[F]–Ru bond has a much reduced magnetic character at low temperatures. In a qualitative discussion, the rhombohedral symmetry of the shared faces splits the threefold-degenerate t orbitals into an a_1 and twofold-degenerate $e_\pm$ orbitals carrying an orbital angular momentum. The a_1 orbital will be half-filled, forming a Ru–Ru homopolar bond, which leaves a localized hole in the $e_\pm^3$ manifold to give a large orbital angular momentum. A strong spin-orbit $\lambda\mathbf{L}\cdot\mathbf{S}$ coupling, which is commonly found in the 4d transition-metal compounds (32), would lead at lowest temperature to a state with J = 0 of the Ru^{4+} ions of a Ru–[F]–Ru pair. The unusual $\chi(T)$ of the 9R phase of $BaRuO_3$, where the Ru–[F]–Ru bonds dominate, can indeed be accounted for quantitatively by taking into account the spin–orbit coupling and spin–spin exchange interaction (32). As for the 6H phase in which 2 of 3 blocks consist of the Ru–[C]–Ru bonds, 3D ferromagnetic coupling is not established and spins are not ordered to the lowest temperatures. It is important to note that an approximately linear fitting of $\chi^{-1}(T)$ within 90 K $< T <$ 240 K for the 6H phase in Fig. 5 may mean a strong antiferromagnetic coupling, as predicted by a Curie–Weiss law, only at higher temperatures, but a suppression by spin–orbit coupling at lower temperatures of the magnetic moment on the Ru^{4+} ions of the Ru–[F]–Ru bonds destroys any long-range magnetic order. More interestingly, $\chi^{-1}(T)$ of 6H phase of $BaRuO_3$ can be seen in Fig. 5 to resemble the essential feature of the χ^{-1}(T) curve of $CaRuO_3$. This observation suggests that the unusual $\chi^{-1}(T)$ found for $CaRuO_3$ and its lack of long-range magnetic order is related to a spin–orbit coupling on the Ru^{4+} ions that suppresses the ferromagnetic spin–spin coupling across the Ru–O–Ru bonds. Narrowing of the π^* band of $SrRuO_3$ by the introduction of the more acidic Ca^{2+} ion and by reducing the Ru–O–Ru bond angle allows removal of the band degeneracy, which enhances the intraatomic spin–orbit coupling $\lambda\mathbf{L}\cdot\mathbf{S}$ to where it competes with the interatomic spin-spin interaction across the Ru–O–Ru bonds having a bond angle much reduced from 180°. In the $Sr_{1-x}Ca_xRuO_3$ system, the reduced bond angle suppresses these Ru–O–Ru interactions to dilute the ferromagnetic interactions so as to give a $\chi^{-1}(T)$ behavior typical of a Griffiths' phase.

In conclusion, we have synthesized the new perovskite $BaRuO_3$ under high pressure, which enables us to map out the evolution of magnetic properties for the perovskite ruthenates. The maximum ferromagnetic Curie temperature $T_c = 164$ K is found for $SrRuO_3$. Substitution of the more ionic and larger Ba^{2+} ion for Sr^{2+} straightens the Ru–O–Ru bond angle and broadens the π^* bandwidth W even where the Ru–O bond is stretched in $BaRuO_3$. The ferromagnetism of the $Sr_{1-y}Ba_yRuO_3$ system can be well described by the Stoner–Wohlfarth model of band ferromagnetism. Substitution of the more acidic and smaller Ca^{2+} ion for Sr^{2+} lowers the Ru–O–Ru bond angles as well as the strength of the interatomic Ru–O–Ru interaction to where the intraatomic spin–orbit $\lambda\mathbf{L}\cdot\mathbf{S}$ coupling competes with the interatomic spin–spin interactions. As a consequence, the ferromagnetic Ru–O–Ru interactions of $SrRuO_3$ become diluted, and the $Sr_{1-x}Ca_xRuO_3$ phase behaves as a Griffiths' phase.

Methods

Synthesis. The starting materials for high-pressure synthesis were prepared by solid-state chemical reaction. The starting materials of $BaCO_3$ (3N), $SrCO_3$ (3N), $CaCO_3$ (3N), and RuO_2 (3N) powders were weighed according to the metal-ion ratio and then thoroughly mixed before sintering at ambient pressure to form single-phase precursors. The single phase of orthorhombic $SrRuO_3$ and $CaRuO_3$ were obtained through solid-state reaction at ambient pressure. The well prepared precursors of $BaRuO_3$ and $Sr_{1-y}Ba_yRuO_3$, which have the 9R polytype structure and a mixture of perovskite and the 9R phase, respectively, were further sintered under high pressure and high temperature. The cubic perovskite $BaRuO_3$ was obtained at 18 GPa at 1,100°C with a KAWAI-type multianvil high-pressure apparatus. The Ba-doped perovskites $Sr_{1-y}Ba_yRuO_3$ $y \leq 0.2$ were made with a cubic high-pressure apparatus under 6 GPa and 1,000°C. The same apparatus has also been used to synthesize the hexagonal polytypes phase of $BaRuO_3$, i.e., the 4H phase $BaRuO_3$ at 1,000°C under 3 GPa, and the 6H phase of $BaRuO_3$ at 1,000°C under 5 GPa. During high-pressure synthesis the samples were held at the targeting pressure and temperature for 30 min before quenching to room temperature followed by release of the pressure.

Crystal Structure Determination. Products of the high-pressure synthesis were characterized by x-ray powder diffraction with a Philips X'pert diffractometer. Diffraction data were collected with 0.02° and 15 s per step. Rietveld analysis has been performed by using the program FullPROF software package.

Measurements of Physical Properties. The magnetic properties of the samples were measured with a superconducting quantum interference device (SQUID) (Quantum Design). The electrical conductivity and thermoelectric power were measured with home-made setups (33). Transport properties under pressure were measured in a piston cylinder high-pressure cell with silicon oil as the pressure medium.

ACKNOWLEDGMENTS. We thank Profs. Z. Fang, G. Cao, and L.Yu for helpful discussions. This work was supported by the National Science Foundation and the Ministry of Science and Technology of China, the National Science Foundation Research Projects 2005CB724402, 2007CB925003, and 50321101, and the Robert A. Welch Foundation of Texas, and the Centers of Excellence project of Japan.

1. Goodenough JB, Zhou JS (1998) Localized to itinerant electron transitions in transition-metal oxides with the perovskite structure. *Chem Mater* 10:2980–2993.
2. Goodenough JB, Longo JM (1970) Crystallographic and magnetic properties of perovskite and perovskite related compounds. *Landolt-Börnstein Numerical Data and Functional Relationships in Science and Technologym*, eds Hellwege K-H, Hellwege AM (Springer, Berlin), Vol III/4, pp 126–314.
3. Goodenough JB, Kafalas JA, Longo JM (1972) High pressure synthesis. *Preparative Methods in Solid State Chemistry*, eds Hagenmuller P (Academic, New York), pp 1–238.
4. Maeno Y, *et al.* (1994) Superconductivity in layered perovskite without copper. *Nature* 372:532–534.
5. Grigera SA, *et al.* (2004) Disorder-sensitive phase formation linked to metamagnetic quantum criticality. *Science* 306:1154–1157.
6. Mao ZQ, *et al.* (2003) Quantum phase transition in quasi-one-dimensional $BaRu_6O_{12}$. *Phys Rev Lett* 90:186601.
7. Longo JM, Raccah PM, Goodenough JB (1968) Magnetic properties of $SrRuO_3$ and $CaRuO_3$. *J Appl Phys* 39:1327–1328.
8. Longo JM, Kafalas JA (1968) Pressure-induced structural changes in the system $Ba_{1-x}Sr_xRuO_3$. *Mater Res Bull* 3:687–692.
9. Klein L, *et al.* (1996) Anomalous spin scattering effects in the badly metallic itinerant ferromagnet $SrRuO_3$. *Phys Rev Lett* 77:2774–2777.
10. Cao G, McCall S, Shepard M, Crow JE, Guertin RP (1997) Thermal, magnetic, and transport properties of single-crystal $Sr_{1-x}Ca_xRuO_3$. *Phys. Rev B* 56: 321–329.
11. Yoshimura K, *et al*. (1999) ^{17}O NMR observation of universal behavior of ferromagnetic spin fluctuations in the itinerant magnetic system $Sr_{1-x}Ca_xRuO_3$. *Phys Rev Lett* 83:4397–4400.
12. He T, Cava RJ (2001) Disorder-induced ferromagnetism in $CaRuO_3$. *Phys Rev B* 63:172403.
13. Allen PB, *et al*. (1996) Transport properties, thermodynamic properties, and electronic structure of $SrRuO_3$. *Phys Rev B* 53:4393–4398.
14. Kim D, *et al.* (2003) Mean-field behavior with Gaussian fluctuations at the ferromagnetic phase transition of $SrRuO_3$. *Phys Rev B* 67:100406.
15. Klein Y, *et al*. (2006) Insensitivity of the band structure of substituted $SrRuO_3$ as probed by Seebeck coefficient measurements. *Phys Rev B* 73:052412.
16. Shikano M, Huang T-K, Inaguma Y, Itoh M, Nakamura T (1994) Pressure dependence of the magnetic transition temperature for ferromagnetic $SrRuO_3$. *Solid State Commun* 90:115–119.
17. Mazin II, Singh DJ (1997) Electronic structure and magnetism in Ru-based perovskites. *Phys Rev B* 56:2556–2571.
18. Donohue PC, Katz L, Ward R (1964) The crystal structure of barium ruthenium oxide and related compounds. *Inorg Chem* 4:306–310.
19. Hong S-T, Sleight AW (1997) Crystal structure of 4H $BaRuO_3$: High pressure phase prepared at ambient temperature. *J Solid State Chem* 128:251.
20. Rijssenbeek JT, *et al*. (1999) Electrical and magnetic properties of the two crystallographic forms of $BaRuO_3$. *Phys Rev B* 59:4561.
21. Shannon RD (1976) Revised effective ionic radii and systematic studies of interatomic distances in halides and chaleogenides. *Acta Crystallogr A* 32:751–767.
22. Fukunaga F, Tsuda N (1994) On the magnetism and electronic conduction of itinerant magnetic system $Ca_{1-x}Sr_xRuO_3$. *J Phys Soc Jpn* 63:3798–3807.
23. Fisher ME, Langer JS (1968) Resistive anomalies at magnetic critical points. *Phys Rev Lett* 20:665–668.
24. Attfield JP (2002) A cation control of perovskite properties. *Cryst Eng* 5:427.
25. Hasegawa H (1980) Single-site spin fluctuation theory of itinerant-electron systems with narrow bends. *J Phys Soc Jpn* 49:178–188.
26. Neumeier JJ, Cornelius AL, Schilling JS (1994) Influence of pressure on the ferromagnetic transition temperature of $SrRuO_3$. *Physica B* 198:324–328.
27. Demuer A, Jaccard DJ, Reiner W, Ahn CH, Triscone J-M (2004) Magnetism of $SrRuO_3$ thin films under high hydrostatic pressure. *Ann Phys (Leipzig)* 13:72–73.
28. He T, Huang Q, Cava RJ (2000) Comparison of the magnetic properties of isoelectronic $Sr_x(Na_{0.5}La_{0.5})_{(1-x)}RuO_3$ and $Sr_xCa_{1-x}RuO_3$ perovskites. *Phys Rev B* 63:24402.
29. Bray AJ (1987) Nature of the Griffiths phase. *Phys Rev Lett* 59:586–589.
30. Griffiths RB (1969) Nonanalytic behavior above the critical point in a random Ising ferromagnet. *Phys Rev Lett* 23:17–19.
31. Stinchcombe RB (1983) *Phase Transition and Critical Phenomena*, eds C. Domb and J.L. Lebowitz (Academic, London), Vol 7, pp 151–183.
32. Drillon M, Padel L, Bernier J-C (1979) Effects of spin-orbit coupling and exchange in $BaRuO_3$. *J Chem Soc Faraday Trans 2* 75:1193–1198.
33. Zhou JS, Goodenough JB, Mitchell JF (1998) Unusual thermoelectric power of single-crystal $La_{1.2}Sr_{1.8}Mn_2O_7$. *Phys Rev B* 58:R579–R582.